"Stars are formed by mergers of dark matter planets": Carl H. Gibson

A detailed mass distribution of a high-density core in Taurus with ALMA

Kazuki Tokuda[1], Toshikazu Onishi[1], Tomoaki Matsumoto[2], Kazuya Saigo[1], Akiko Kawamura[3], Yasuo Fukui[4], Shu-ichiro Inutsuka[4], Masahiro N. Machida[5], Kengo Tomida[6], Kengo Tachihara[4], and Philippe André[7]

Received _____; accepted _____

Not to appear in Nonlearned J., 45.

[1]Department of Physical Science, Graduate School of Science, Osaka Prefecture University, 1-1 Gakuen-cho, Naka-ku, Sakai, Osaka 599-8531, Japan

[2]Faculty of Humanity and Environment, Hosei University, Fujimi, Chiyoda-ku, Tokyo 102-8160, Japan

[3]National Astronomical Observatory of Japan, Mitaka, Tokyo 181-8588, Japan

[4]Department of Astrophysics, Nagoya University, Chikusa-ku, Nagoya 464-8602, Japan

[5]Department of Earth and Planetary Sciences, Kyushu University, Fukuoka 819-0395, Japan

[6]Department of Earth and Space Science, Graduate School of Science, Osaka University, 1-1 Machikaneyama, Toyonaka, Osaka 560-0043, Japan

[7]Laboratoire AIM, CEA/DSM-CNRS-Université Paris Diderot, IRFU/Service d'Astrophysique, C.E. Saclay, Orme des Merisiers, 91191, Gif-sur-Yvette, France

ABSTRACT

We present the results of ALMA observations of dust continuum emission and molecular rotational lines, including the ALMA Compact Array, toward a dense core MC27 (a.k.a. L1521F) in Taurus, which is considered to be at very early stage of star formation. Detailed column density distribution with a size scale from a few tens AU to ~10000 AU scale are revealed by combining the ALMA data and the single-dish data. The high angular resolution observation at 0.87 mm reveals that a protostellar source, MMS-1, is still not spatially resolved without gas association and a starless high-density core, MMS-2, has substructures both in dust and molecular emission. The averaged radial column density distribution of the inner part ($r \lesssim 3000$ AU) is $N_{\rm H_2} \sim r^{-0.4}$, clearly flatter than that of the outer part, $\sim r^{-1.0}$. We found the complex velocity/spatial structure obtained with previous ALMA observations is located inside the inner flatter region, which may reflect the dynamical status of the dense core.

Subject headings: ISM:clouds — ISM: kinematics and dynamics — ISM: molecules — stars: formation

This is a "cold core" region, with temperatures ~ 14 K reflecting the evaporation of frozen dark matter planets.

~10^16 m: which is the Oort cavity diameter of all stars in HGD cosmology.

Formation of stars from dark matter planets is revealed for the first time in these ALMA observations.

1. Introduction

An observational study of the earliest stage of star-formation is a key to pursue the initial conditions of star formation, e.g., the way of the fragmentation and the dynamical collapse. Recent observations suggest that individual protostellar collapse often leads to multiple protostellar systems (e.g., Chen et al. 2013), although not as often as in purely hydrodynamic simulations and confusion by small-scale structure in the associated protostellar outflow(s) is sometimes an issue (Maury et al. 2010). Complex gas structures have also been observed in the envelopes on spatial scales from 0.1pc to ∼1000 AU (Tobin et al. 2010, 2011). It is thus of vital importance to reveal the fragmentation process of a dense core to form multiple stars therein. In spite of a number of observational efforts made thus far, some of the most fundamental issues are still left without good answers. Especially, an observational missing link between the complex envelope and formed protostars has still remained. The observations revealing how the surrounding gas interacts to form stars at the center of a dense core is a key to understand the origin of binary or multiple systems. Previous interferometric observations with high angular resolutions failed to detect extended high-density gas around protostars due to the lack of the sensitivity and the narrow spatial frequency coverage. The recent ALMA observations have been revealing the detailed structure of the innermost region of dense cores where multiple protostars are currently forming. MC27 (Mizuno et al. 1994; Onishi et al. 1996, 1998, 1999, 2002) or L1521F (Codella et al. 1997) is one of the densest cores in Taurus. It was considered as a prestellar core, until *Spitzer* observations (Bourke et al. 2006) have detected a very low-luminosity (<0.07 $L_\odot$) protostar (hereafter, the *Spitzer* source). It is of very high density and contains the *Spitzer* source, which indicates it is among the youngest known Class 0 protostars (cf. André et al. 2000) and still may preserve the initial conditions of star formation (Bourke et al. 2006; Terebey et al. 2009). Tokuda et al. (2014) recently carried out ALMA Cycle 0 observations

No, this is not the way stars are formed.

All stars form by a sequence of dark matter planet mergers.

At 30 kyr the density was 10^10 cm^-3, or 10^-17 kg m^-3.

The high density is a fossil of the density existing in the plasma epoch when proto-galaxies fragmented at a time 10^12 seconds after the big bang.

toward the object at an angular resolution of $\sim$1″ by using the 12-m array, and revealed that the spatial and velocity distributions are very complex. We detected (1) a few starless high-density condensation ($\sim 10^7$ cm^{-3}), within a regions of a several hundred AU around the *Spitzer* source, (2) a very compact bipolar outflow centered at the *Spitzer* source with a dynamical time of a few hundred years with an indication of interaction of surrounding gas, and (3) a well-defined long arc-like structure whose size is $\sim$2000 AU. Subsequent numerical simulations demonstrate that a dense core undergoes gravitational collapse to form multiple protostars and gravitational torque from orbiting protostars create arc structures extending up to a thousand AU scale (Matsumoto et al. 2015). These studies have been suggested that dynamical gas interactions are a key to form the multiple (or binary) protostars.

In spite of these new findings with ALMA, there is a gap of the coverage of the spatial frequencies between single dish observations with large aperture telescopes and the 12-m array of ALMA. Therefore, additional investigations were really needed to understand the mechanism creating the above-mentioned complex structures and how protostars form in such an environment.

One of the best methods to diagnose the evolutionary status of dense cores is to investigate the mass distribution because it should regulate the dynamics of cores. In Taurus, Onishi et al. (2002) suggested that the peak density of 10^6 cm^{-3}, by measuring with a beam size of $\sim$20″, would be a threshold for the dynamical collapse. When the first core is formed, the density should continuously increase to the center probably in a form of $n_{\rm H_2} \sim r^{-2}$ (e.g., Larson 1969; Masunaga et al. 1998). The finest beam size that can be achieved by single dish telescopes is currently $\sim$11″ by MAMBO-2 (Kreysa et al. 1999) or a new-generation continuum camera "NIKA2"(Calvo et al. 2016) observations with the IRAM 30-m telescope, and the ALMA 12-m array cannot cover well the angular extent above several arcseconds. The mass distribution inside the beam size of $\sim$10″, corresponding to a spatial scale of 1400 AU at a distance of Taurus (140 pc; e.g., Elias et al. 1978), is

Wrong mechanism for star formation.

very important to know the evolution because most of the stellar mass is included in the radius. Recently, an approach that combines data obtained with single-dish telescopes and interferometers has been widely used to investigate the physical properties in protostellar systems (e.g., B335, Yen et al. 2011; Kurono et al. 2013). ALMA has a capability to obtain the shorter spatial frequencies filling the gap between the single dish and the 12-m array by using the ACA (Atacama Compact Array; Morita array).

In this paper, we present the results of higher resolution observations in frequency Band 7 with ALMA to reveal the detailed structure of the central part of the core. We then show the dust mass distribution, derived from 1.1 mm continuum observations, continuously from ∼100 AU to ∼10000 AU by combining the data taken with ALMA 12-m array, ALMA ACA 7-m array, and the IRAM 30-m/MAMBO-2.

2. Observations

We carried out ALMA Cycle 1 Band 6 (211–275 GHz) and Band 7 (275–373 GHz) observations toward MC27/L1521F at the center position of ($\alpha_{J2000.0}$, $\delta_{J2000.0}$) = ($4^{\rm h}28^{\rm m}39\overset{\rm s}{.}00$, $+26^\circ51'35\overset{''}{.}0$) with the 12-m array and the 7-m array (ACA). The observations have been carried out between 2013 October and 2015 June. The correlator was used in the frequency domain mode with a bandwidth of 1875 MHz (488 kHz 3840 channels) in each spectral window. The total bandwidth is 7.5 GHz in each observation. The basebands in Band 6 include e.g., CS (J = 5–4) and $H^{13}CO^+$ (J = 3–2) and those in Band 7 include e.g., $C^{17}O$ (J = 3–2), ^{12}CO (J = 3–2) and $H^{13}CO^+$ (J = 4–3). The uv distances of the Band 6 and Band 7 with the 12-m array data are 10.9–239 kλ and 16.2–699 kλ, respectively. The 7-m array data of the Band 6 and the Band 7 cover the baseline ranges of 8.1–27.7 kλ and 8.9–43.9 kλ, respectively. The calibration of the complex gains was carried out through observations of 4 quasars (J0423-0120, J0510-0159, J0532+0732 and J0238+1636),

phase calibration of 2 quasars (J0510+1800 and J0438+3004), and flux calibration of 2 solar system objects (Ganymede and Uranus) and a quasar (J0510+1800). For the flux calibration of the solar system objects, we used the Butler-JPL-Horizons 2012 model (https://science.nrao.edu/facilities/alma/aboutALMA/Technology/ALMA_Memo_Series /alma594/abs594). The data were reduced using the Common Astronomy Software Application package (http://casa.nrao.edu) and the visibility imaged. We used the natural weighting for both the Band 6 and the Band 7 data. The provided value of the synthesized beams and the sensitivities are listed in Table 1.

Continuum observations of the 1.2 mm thermal dust emission were done in February 2003 with the IRAM 30-m telescope on Pico Veleta (Spain) using 117-receiver MAMBO-2 bolometer (240″diameter) cameras of the Max-Planck-Institute Radioastronomie (Kreysa et al. 1999). The beam size on the sky was 11″, and the effective frequency 250 GHz with half sensitivity limits at 210 and 290 GHz. Pointing and focus position were usually checked before and after each map.

3. Results

3.1. High resolution observations of the central part of high-density dust cores

Figure 1 shows that the present Band 7 continuum observations detected three intensity peaks, and they correspond to MMS-1, MMS-2, and MMS-3 identified with the previous Band 6 continuum observations (Tokuda et al. 2014). MMS-1, which coincides with the *Spitzer* source, is not spatially resolved even with the current angular resolution of $\sim$0.″74 0.″34, which is consistent with the PdBI observations by Maury et al. (2010). The deconvolved size is 0.″28±0.″1 × 0.″13±0.″06, corresponding to 40±14 AU × 18±8 AU. We have not detected significant molecular line emission enhancements toward MMS-1 in ^{12}CO (J = 3–2), H^{13}CO$^+$ (J = 4–3), and C^{17}O (J = 3–2), indicating that the *Spitzer*

source does not have extended gas envelopes. However, the dust emission and the compact outflow emitted from MMS-1 implies the existence of a disk-like envelope around the central protostar, and thus further high angular resolution observations are definitely needed to investigate the nature and evolutionary stage of MMS-1.

The spatial distribution of Band 7 continuum is similar to that of Band 6, and the sizes of the whole extent of MMS-2 are almost the same of ∼360 AU at Band 6 and Band 7. The Band 7 continuum observation revealed that MMS-2 could be further resolved into two peaks. This fact is also supported by the spatial distribution of molecular line emissions of $C^{17}O$ (J = 3–2). On the other hand, the spatial distribution of $H^{13}CO^+$ (J = 4–3) emission shows the single peaked distribution. This may be because the line is too optically thick to probe the central part in MMS-2; $H^{13}CO^+$ (J = 3–2) spectra were also suggested to be optically thick (Tokuda et al. 2014). Actually, the integrated intensity ratio of $H^{13}CO^+$ (J = 4–3)/$H^{13}CO^+$ (J = 3–2) around the $H^{13}CO^+$ (J = 4–3) peak in MMS-2 reached ∼0.8, indicating that the $H^{13}CO^+$ (J = 4–3) is fully thermalized and that the region should be very high-density of $>10^7$ cm^{-3} with a calculation by a non-LTE analysis (RADEX; van der Tak et al. 2007) under the assumption of the kinematic temperature of 10 K.

Another dust core, MMS-3 is located toward the north-west of the *Spitzer* source with ∼3σ detection. The $C^{17}O$ (J = 3–2) emission was not detected, but the $H^{13}CO^+$ (J = 4–3) emission detected toward this source. The integrated intensity ratio of $H^{13}CO^+$ (J = 4–3)/$H^{13}CO^+$ (J =3–2) is ∼0.5, which corresponds with a density of $\sim 10^6$ cm^{-3} from the non-LTE calculation, and then the MMS-3 is less dense than MMS-2 by a factor of ∼10. Non-detection of $C^{17}O$ (J = 3–2) is justified by the fact that the optically thin $C^{17}O$ (J = 3–2) traces the column density and that the column density derived from the continuum emission is less than half of the MMS-2 as shown below.

We derived the total mass and the column density from the 0.87 mm dust continuum data to investigate the physical properties of the condensations with assumption of optically

thin emission and uniform dust temperature. The column density of molecular hydrogen is estimated by using

$$N_{\rm H_2} = F_\nu^{\rm beam}/\Omega_{\rm A}\mu_{\rm H_2}m_{\rm H}\kappa_\nu B_\nu(T_{\rm d}) \quad (1)$$

and,

$$\kappa_\nu = \kappa_{231{\rm GHz}}(\nu/231{\rm GHz})^\beta \quad (2)$$

where $F_\nu^{\rm beam}$ is the flux per beam at frequency ν, $\Omega_{\rm A}$ is the solid angle of the beam, $\mu_{\rm H_2}$ is the molecular weight per hydrogen, $m_{\rm H}$ is the H-atom mass, κ_ν is the mass absorption coefficient, $\kappa_{231{\rm GHz}} = 1.0 \times 10^{-2}$ cm^2 g^{-1} of interstellar matter is the emissivity of the dust continuum at 231 GHz (Ossenkopf & Henning 1994; Kauffmann et al. 2008), β is the dust emissivity index, B_ν is the Plank function and $T_{\rm d}$ is the dust temperature. To estimate the total mass ($M_{\rm total}$), we use

$$M_{\rm total} = F_\nu d^2/\kappa_\nu B_\nu(T_{\rm d}) \quad (3)$$

where F_ν the integrated flux of the continuum emission at frequency ν and d is the distance of the source (140 pc; Elias 1978). We assumed $T_{\rm d} = 10$ K, which is consistent with the spectral energy distribution of MC27/L1521F observed with *Herschel* as part of the Gould Belt survey (Andé et al. 2010; P. Palmeirim PhD thesis, private communication). β was assumed to be 1.9, which is the average value derived from the ratios of 250 GHz and 345 GHz intensities ranging from 1.7 to 2.1, and this value is consistent with those assumed for radiative transfer models of Class 0 envelopes (Ossenkopf & Henning 1994) and other Class 0 observations (Shirley 2011). The mass absorption coefficient at 345 GHz is thus calculated to be $\kappa_{345{\rm GHz}}$= 2.1 $\times$ 10^{-2} cm^2 g^{-1}. The derived parameters of the dust sources are shown in Table 2. The parameters are consistent with the results derived from the 1.1 mm dust continuum data (Tokuda et al. 2014) within ∼10–20% for MMS-2. We note here that larger difference is seen toward MMS-3 by a factor of 2–3. This may be because the emission toward MMS-3 is almost 3σ detections in both frequencies, and thus the error in the intensities are considered not to be small.

3.2. Detailed column density distribution toward MC27

Two figures in Figure 2 demonstrate the distributions of the Band 6 continuum observed by the 12-m array and 7-m array. The 7-m array and IRAM 30-m data in Figure 3 show the single peaked core centered around MMS-1 and MMS-2, and the 12-m array data resolved the complex structure at the innermost region. The total flux obtained by the 12-m array observation in the observed area is ∼21 mJy, which is smaller than that by the 7-m array in the same area of ∼61 mJy, and even smaller than IRAM 30-m data of ∼200 mJy. This fact indicates that the 12-m array observations missed a significant amount of flux of the extended emission, and even the 7-m array observations have the same situation. Therefore, we combined the three different datasets by using the feathering technic in an accordance with the CASA instruction obtained by ALMA; we cleaned the 7-m and 12-m datasets individually and combined the cleaned maps and the single-dish map in Fourier space.

Figure 3(a) shows the dust continuum image obtained by the IRAM 30-m/MAMBO-2. Figure 3(b) is the combined image of the three dataset. We obtained the column density with the equation (2) by assuming $T_d = 10$ K and $\kappa_\nu = 1.2 \times 10^{-2}$ cm^2 g^{-1} (Ossenkopf & Henning 1994; Kauffmann et al. 2008). The synthesized beam size is $1\farcs3 \times 0\farcs8$. The complex structure is actually seen around the peak of the extended core emission. The noise-like ragged structure seen in the envelope comes from the fact that the 7-m array and IRAM 30-m dataset do not have sufficient sensitivities for the beam size.

Figure 4 (a) and (b) show a comparison between the dust continuum emissions of the Band 6 and those of the Band 7. We used the JCMT/SCUBA data obtained by Shinnaga et al. (2004) and Kirk et al. (2005) as a single-dish data. The combined image of the Band 7 were generated by the same technique as described above. Both Figure 4 (a) and (b) roughly show the same spatial distributions, indicting that they are tracing the same gas/dust component. We note that the relative flux intensity ratio of the Band 6 to the Band 7

toward MMS-1 is relatively weak compared to the other part. The dust emissivity index, β is $\sim$0.4, indicating that MMS-1 is optically thicker than the extended envelopes and/or starless dense cores (MMS-2, MMS-3).

Figure 5 shows the mean radial profile of the H_2 column densities centered at MMS-2 derived from the Band 6 observations. Even if we change the center to MMS-1, the change in the radial profile is very small and does not affect the discussion below. The radial profile derived from Band 7 is quite similar to that from Band 6, and thus we use only the Band 6 data to investigate the mass distribution. The radial profile seems to be a combination of multiple slopes. The inner part has a slope of $\sim r^{-0.4}$, and the outer part has a steeper slope of $\sim r^{-1.3}$. We note here that the dual-beam on-the-fly mapping mode of the MAMBO-2, which was used for the present observations, suffers from a progressive loss of signal as angular radius increases (Motte & André 2001). Therefore, the slope of the outer part is expected to be shallower than the observed radial profile. A simulation, similar to that described in the Appendix of Motte & André (2001), indicates that the observed radial profile is consistent with an intrinsic column density distribution $\sim r^{-1.0\pm0.2}$ beyond $\sim$3000 AU and up to $\sim$14000 AU. Therefore, the steep slope of $N_{\rm H_2} \sim r^{-1.0}$, corresponding to a density distribution $n_{\rm H_2} \sim r^{-2.0}$, which was observed in previous studies (Onishi et al. 1999; Tatematsu et al. 2004; Crapsi et al. 2004) actually ends below $\sim$3000 AU.

We note that we detected a Band 6 continuum peak toward ($\alpha_{J2000.0}$, $\delta_{J2000.0}$) = ($4^{\rm h}28^{\rm m}37\overset{\rm s}{.}84$, $+26^\circ51'28\overset{''}{.}4$) (Figure 2(b)). We detected the source both in Cycle 0 and Cycle 1 observations. The total flux is measured to be $\sim$1 mJy $1\overset{''}{.}3 \times 0\overset{''}{.}8$ beam^{-1}, and there is no corresponding gas emission detected toward the peak. One possibility is that the source is a YSO older than the protostar phase although we cannot find corresponding stars in the *Spitzer* and optical data. Then, the most probable candidate is a distant external galaxy.

3.3. Distributions of surrounding gas traced by ^{12}CO (J = 3–2)

The ^{12}CO (J = 3–2) line can be used to trace the lower-density gas compared with the other molecular lines in which we observed in Cycle 0 and Cycle 1. Figure 6 shows the channel maps of the ^{12}CO (J = 3–2) observations with the 12-m array alone with contours of HCO$^+$ (J = 3–2) of the Cycle 0 observations. The ^{12}CO (J = 3–2) intensity map at 5 km s^{-1} is tracing filamentary/core-like structures and is very similar to that in HCO$^+$ (J = 3–2). However, at 7 km s^{-1}, the ^{12}CO (J = 3–2) emission is not detected although HCO$^+$ (J = 3–2) shows the characteristic filamentary structure which was shown in Tokuda et al. (2014) as an indication of the dynamical interaction of dense gas. This behavior can be explained by the extremely large optical depth of ^{12}CO (J = 3–2) compared with HCO$^+$ (J = 3–2). The spectral profile in black in Figure 7(b) is the averaged spectrum of the ^{12}CO (J = 3–2) over the region where the line is detected. It is clear that the there is a clear dip at the velocities higher than $\sim$ 6 km s^{-1}, and this dip can be interpreted as the optical thickness of the line. The intensity enhancement of HCO$^+$ (J = 3–2) at 3 km s^{-1} is a part of the outflow from the *Spitzer* source (Tokuda et al. 2014), and we obtained the ^{12}CO (J = 3–2) emission toward the region at the same velocity. The profile in blue in Figure 7(b) is the averaged ^{12}CO (J = 3–2) spectrum toward the region, and there is a clear indication of the blueshifted component of the outflow even in ^{12}CO (J = 3–2). Figure 7(a) shows that the distributions of the blue wing component are almost the same both in ^{12}CO (J = 3–2) and HCO$^+$ (J = 3–2). However, the ^{12}CO (J = 3–2) emission was not detected toward the region where we detected the red wing component of the bipolar outflow detected in HCO$^+$ (J = 3–2) by Tokuda et al. (2014). This may be due to the optical thickness of the ^{12}CO (J = 3–2) line at the velocity range. Actually, the ^{12}CO (J = 3–2) intensity of 7–9 km s^{-1} is very weak as shown in Figure 7(b) although the single dish observations revealed strong emission at the same velocity range (Takahashi et al. 2013).

4. Discussion

4.1. Density profile

The continuum distributions and the detailed radial column density profiles were presented in Sec. 3.2. First, we will summarize the past studies for the radial (column) density profiles toward protostellar and/or prestellar cores based on the (sub-)millimeter continuum observations and compare them with our present results toward MC27/L1521. MC27/L1521F is regarded as a dense core at a protostellar stage. However, the luminosity of the source is quite low (Bourke et al. 2006) and the envelope of the protostar has a large amount of gas, indicating that the system preserves the initial condition of the protostar formation. We here compare the density profiles of MC27/L1521F with the past observational studies of prestellar/protostellar cores to investigate the evolutionary status. Previous (sub-)millimeter continuum observations toward Class 0/I sources in Taurus (e.g., Motte & André 2001; Chandler & Richer 2000; Shirley et al. 2000) have revealed that the density profiles of the protostellar cores show $\rho(r) \propto r^{-p}$ with p ∼1.5–2.0 over ∼10000–15000 AU in radius. Ward-Thompson et al. (2007) mentioned that the protostellar envelopes are more centrally condensed than prestellar cores and do not show the inner flattering in their radial column density profiles. These results are roughly consistent with the predictions of the isolated star formation model (e.g., Shu 1977). Kirk et al. (2005) obtained similar results toward a number of (∼30) prestellar cores, and categorized them into two groups, 'bright' cores and 'intermediate' cores, based on their flux intensities of the submillimeter continuum emissions. They found that intermediate cores are in agreement with a Bonner-Ebert sphere (see also Alves et al. 2001). On the other hand, in bright cores, the critical Bonner-Ebert sphere is not consistent with the radial density profiles of the cores, suggesting that they are already collapsing, or there is some additional mechanism (e.g., magnetic field) to support the cores. MC27/L1521F was characterized as the bright

core of their work. The flattering radius ($R_{\rm flat}$) measured with 850 μm data is 3400 AU. Recent multi-wavelength studies obtained by *Herschel* space observatory (Launhardt et al. 2013) determined the radial profiles of the column density and the temperature toward both protostellar cores and prestelaller cores and imply that the column density profiles are flat toward the peak. Roy et al. (2014) also discussed similar results toward two prestellar cores (B68 and L1689B). High angular resolution observations with the interferometer combining the single-dish data have revealed that the density profiles of Class 0 source follows multiple power low. Harvey et al. (2003a,b) derived the density profile of B335 core, containing a confirmed Class 0 source with a broken power low with a shallow density profile inside $\sim$6500 AU, $n(r) \propto r^{-1.5}$ and $r^{-2.0}$ outside (see also Kurono et al. 2013). Kurono et al. (2013) mentioned that the profile follows the inside-out collapse model (e.g., Shu 1977). The present ALMA data on MC27/L1521F shows that the radial profile of the density seems to be a combination of at least two slopes; steeper outside and shallower inside as presented in section 3.2. Inside 3000AU, the density slope is $n_{\rm H_2}\sim r^{-1.5}$, which mimics the slope that is expected in the region where the inside-out collapse is occurring as is in the case of B335 above. The inside-out collapse expands outwards with a velocity of the sound speed, $\sim$0.2 km s^{-1} at 10 K (Shu 1977), and thus it takes $\sim 7\times10^4$ years to reach the 3000 AU. However, the extreme faintness of the infrared source and quite short dynamical time of the outflow of a few hundreds years (Tokuda et al. 2014) imply that the infrared source is at the very early stage of protostar formation, much earlier than 7×10^4 years. Moreover, the observed gas velocity shown in Figure 6 indicate a complex structure rather than a coherent infall motion owing to the inside-out collapse. Therefore, the shallow slope of the radial profile of the density is not probably attributed for the inside-out collapse in the case of MC27/L1521F. A possible scenario is that the shallow slope of the radial density profile is a consequence of a dynamical interaction between the high-density condensations and the envelopes because the region showing the shallow slope overlaps with the region

existing the complex structures, such as arc-like structures. As shown in the channel maps of Figure 6, the velocity of the complex structures ranges in $\sim \pm 1$ km s^{-1} with respective to the systemic velocity. The time scale for disturbance to propagate to a 3000 AU scale is estimated to be 1.4×10^4 yr ($=$ 3000 AU/1 km s^{-1}), which is consistent with an age of the protostar in the early phase.

According to dust continuum emission obtained by combining the ALMA 12-m array and 7-m array with IRAM 30-m, the total mass of the gas within $r \lesssim 3000$ AU is estimated as $M_{\rm gas} = 0.49\,M_\odot$, yielding a typical dynamical velocity of 0.4 km s^{-1} ($= [GM_{\rm gas}/3000\ {\rm AU}]^{1/2}$). This velocity is significantly lower than the observed velocity of 1 km s^{-1}, and this implies that the gas flow on this scale is caused by a dynamical interaction on the smaller scale. Matsumoto et al. (2015) demonstrates that a dynamical interaction on a 100 AU scale disturbs the envelopes on a $\sim$1000 AU scale, reproducing the arc-like structure on that scale.

4.2. Envelope structure seen in ^{12}CO (J = 3–2)

Takahashi et al. (2013) claimed that they detected molecular outflows in ^{12}CO (J = 2–1) line with the SMA; one is originated from the *Spitzer* source, and another is from the unknown source. They said that the blueshifted CO emission is brighter on the eastern side, which is in the opposite sense to what might be expected from the reflection nebula image obtained by the *Spitzer* observations (Bourke et al. 2006; Terebey et al. 2009). Their speculation of the cause is a consequence of the non-uniform distribution of the surrounding material. On the other hand, Tokuda et al. (2014) detected a compact outflow in HCO$^+$ (J = 3–2) with ALMA, and the direction of the outflow is consistent with the *Spitzer* reflection nebula. In addition to this, we detected the blue wing component in ^{12}CO (J = 3–2) in the present observations, which coincides with that in HCO$^+$ (J = 3–2). Here we

check the SMA outflows with the present ALMA observations in ^{12}CO (J = 3–2) line. It is clear that they have not detected the outflowing gas corresponding to the HCO$^+$ (J = 3–2) outflow because the extent is quite small of $\sim$2″. If we spatially smooth the angular resolution of the channel maps in Figure 6 to the SMA resolution of Takahashi et al. (2013), the ^{12}CO (J = 2–1) and ^{12}CO (J = 3–2) distributions are quite similar, indicating that both observations are tracing the same gas. The blueshifted velocity component of Figure 2 of Takahashi et al. (2013) is seen mainly at 5 km s^{-1} in Figure 6, and they are actually filaments/cores that are also seen in HCO$^+$ (J = 3–2) with the velocity range from 4 to 7 km s^{-1}. Similar structure is also seen in H^{13}CO$^+$ (J = 3–2) as shown in Figure 1 of Tokuda et al. (2014). Therefore, this blueshifted velocity component is not the high-velocity gas from the outflow, but relatively high-density gas structure at the center of this object. The redshifted velocity component seems to be a bit complicated. The ^{12}CO cloud at ($\alpha_{J2000.0}$, $\delta_{J2000.0}$) = ($4^{\rm h}28^{\rm m}39\overset{\rm s}{.}21$, $+26^\circ51'36\overset{''}{.}1$) corresponds to the HCO$^+$ (J = 3–2) cloud possibly interacting with the HCO$^+$ (J = 3–2) outflow that is shown in red-dashed contours in Figure 2 (b and c) of Tokuda et al. (2014). We thus conclude that the blueshifted and redshifted components in ^{12}CO (J = 2–1) in Takahashi et al. (2013) are not representing the outflowing gas emitted from the protostars, but a part of the complex dense gas structure in the core.

5. Summary

We present new interferometric dust continuum and molecular line observations of the dense core MC27/L1521F, containing a very faint protostar made with the ALMA Cycle 1 at wavelengths of 1.1 and 0.87 mm, including the Atacama Compact Array (ACA, a.k.a. Morita Array). We combine these data with previous dust continuum observations obtained by single-dish telescopes. Our main results are summarized as follows.

1. High angular resolution ($\sim$0$''$.3) observations with ALMA Band 7 (0.87 mm) show that MMS-1, the faintest protostar (the *Spitzer* source) is still not spatially resolved and MMS-2, a starless high-density ($>10^7$ cm^{-3}) core is further resolved into two peaks. Further high-angular resolution observations with the long-baseline configurations would be anticipated to reveal the detailed evolutionary stages of these sources.
2. Detailed column density distribution with the size from $\sim$100 to $\sim$10000 AU scale are revealed by combining the 12-m array (Main array) data with the 7-m array (ACA) data as well as with the single dish IRAM/MAMBO-2 or JCMT/SCUBA data. The spatial dynamic range is significantly improved by an order of magnitude compared to previous studies. Our analysis shows that the averaged radial column density distribution of the inner part ($r < 3000$ AU) is $N_{\rm H_2} \sim r^{-0.4}$, clearly flatter than that of the outer part, $\sim r^{-1.0}$. We detected the complex structure presented by previous ALMA observations (Tokuda et al. 2014) inside the inner flatter region, which may reflect the dynamical status of the dense core.
3. We compared our ^{12}CO (J = 3–2) data with previous ^{12}CO (J = 2–1) data taken by the SMA (Takahashi et al. 2013). We concluded that the ^{12}CO redshifted and blueshifted velocity component observed by Takahashi et al. (2013) are not outflowing gases ejected from the protostellar sources but a part of the complex gas structure.

This paper makes use of the following ALMA data:ADS/JAO.ALMA#2011.0.00611.S and 2012.1.00239.S. ALMA is a partnership of the ESO, NSF, NINS, NRC, NSC, and ASIAA. The Joint ALMA Observatory is operated by the ESO, AUI/NRAO, and NAOJ. This work was financially supported by the Japan Society for the Promotion of Science (JSPS) KAKENHI grant Nos. 22244014, 23403001, 23540270, 24244017, 26247026, 26287030 and 26400233. K. Tokuda is supported by a JSPS Research Fellow.

T. Onishi supported by the ALMA Japan Research Grant of NAOJ Chile Observatory, NAOJ-ALMA-0013 and NAOJ-ALMA-0032. Ph. André is partly supported by the European Research Council under the European Union's Seventh Framework Programme (ERC Grant Agreement no. 291294). This work is partly based on observations carried out with the IRAM 30m Telescope. IRAM is supported by INSU/CNRS (France), MPG (Germany) and IGN (Spain).

The authors of this very interesting paper seem to be unaware that it is an observational fact that all stars are formed by mergers of dark matter planets in PGC clumps of a trillion: ie HGD cosmology.

REFERENCES

Alves, J. F., Lada, C. J., & Lada, E. A. 2001, Nature, 409, 159

André, P., Men'shchikov, A., Bontemps, S., et al. 2010, A&A, 518, L102

André, P., Ward-Thompson, D., & Barsony, M. 2000, in Protostars and Planets IV, ed. V. Mannings, A. P. Boss, & S. S. Russell (Tucson, AZ: Univ. Arizona Press), 59

Bourke, T. L., Myers, P. C., Evans, N. J., II, et al., 2006, ApJ, 649, L37

Calvo, M., Benoit, A., Catalano, A., et al. 2016, arXive:1601.02774

Chandler, C. J., & Richer, J. S. 2000, ApJ, 530, 851

Chen, X., Arce, H. G., Zhang, Q., et al. 2013, ApJ, 768, 110

Crapsi, A., Caselli, P., Walmsley, C. M., et al. 2004, A&A, 420, 957

Codella, C., Welser, R., Henkel, C., Benson, P. J., & Myers, P. C. 1997, A&A, 324, 203

Elias, J. H. 1978, ApJ, 224, 857

Harvey, D. W. A., Wilner, D. J., Myers, P. C., & Tafalla, M. 2003a, ApJ, 596, 383

Harvey, D. W. A., Wilner, D. J., Myers, P. C., Tafalla, M., & Mardones, D. 2003b, ApJ, 583, 809

Kauffmann, J., Bertoldi, F., Bourke, T. L., Evans, N. J., II, & Lee, C. W. 2008, A&A, 487, 993

Kirk, J. M., Ward-Thompson, D. & André, P. 2005, MNRAS, 360, 1506

Kreysa, E., Gemünd, H.-P., Gromke, J. et al. 1999, Infrared Physics & Technology, 40, 191

Kurono, Y., Saito, M., Kamazaki, T., Morita, K., & Kawabe, R. 2013, ApJ, 765, 85

Larson, R. B. 1969, MNRAS, 145, 271

Launhardt, R., Stutz, A. M., Schmiedeke, A., et al. 2013, A&A, 551, A98

Masunaga, H., Miyama, S. M., & Inutsuka, S. 1998, ApJ, 495, 346

Matsumoto, T., Onishi, T., Tokuda, K., & Inutsuka, S. 2015, MNRAS, 449, L123

Maury, A. J., André, P., Hennebelle, P., et al. 2010, A&A, 512, A40

Mizuno, A, Onishi, T., Hayashi, M., et al., 1994, Nature, 368, 719

Motte, F., & André, P. 2001, A&A, 365, 440

Onishi, T., Mizuno, A., Kawamura, A., Ogawa, H., & Fukui, Y. 1996, ApJ, 465, 815

Onishi, T., Mizuno, A., Kawamura, A., Ogawa, H., & Fukui, Y. 1998, ApJ, 502, 296

Onishi, T., Mizuno, A., & Fukui, Y. 1999, PASJ, 51, 257

Onishi, T., Mizuno, A., Kawamura, A., Tachihara, K., & Fukui, Y. 2002, ApJ, 575, 950

Ossenkopf, V., & Henning, T. 1994, A&A, 291, 943

Roy, A., André, P., Palmeirim, P., et al. 2014, A&A, 562, 138

Shinnaga, H., Ohashi, N., Lee, S.-W., & Moriarty-Schieven, G. H. 2004, ApJ, 601, 962

Shirley, Y. L., Evans, N. J., II, Rawlings, J. M. C., & Gregersen, E. M. 2000, ApJS, 131, 249

Shirley, Y. L., Mason, B. S., & Mangum, J. G., et al. 2011, AJ, 141, 39

Shu, F. H. 1977, ApJ, 214, 488

Takahashi, S., Ohashi, N., & Bourke, T. L. 2013, ApJ, 774, 20

Tatematsu, K., Umemoto, T., Kandori, R., & Sekimoto, Y. 2004, ApJ, 606, 333

Terebey, S., Fich, M., Noriega-Crespo, A., et al. 2009, ApJ, 696, 1918

Tobin, J. J., Hartmann, L., Chiang, H., et al. 2011, ApJ, 740, 45

Tobin, J. J., Hartmann, L., Looney, L. W., & Chiang, H. 2010, ApJ, 712, 1010

Tokuda, K., Onishi, T., Saigo, K., et al. 2014, ApJ, 789, L4

Yen, H.-W., Takakuwa, S., & Ohashi, N. 2011, ApJ, 742, 57

van der Tak, F. F. S., Black, J. H., Schöier, F. L., Jansen, D. J., & van Dishoeck, E. F. 2007, A&A, 468, 627

Ward-Thompson, D., André, P., Crutcher, R., et al. 2007, in Protostars and Planets V, ed. B. Reipurth et al. (Tucson, AZ: Univ. Arizona Press), 951, 33

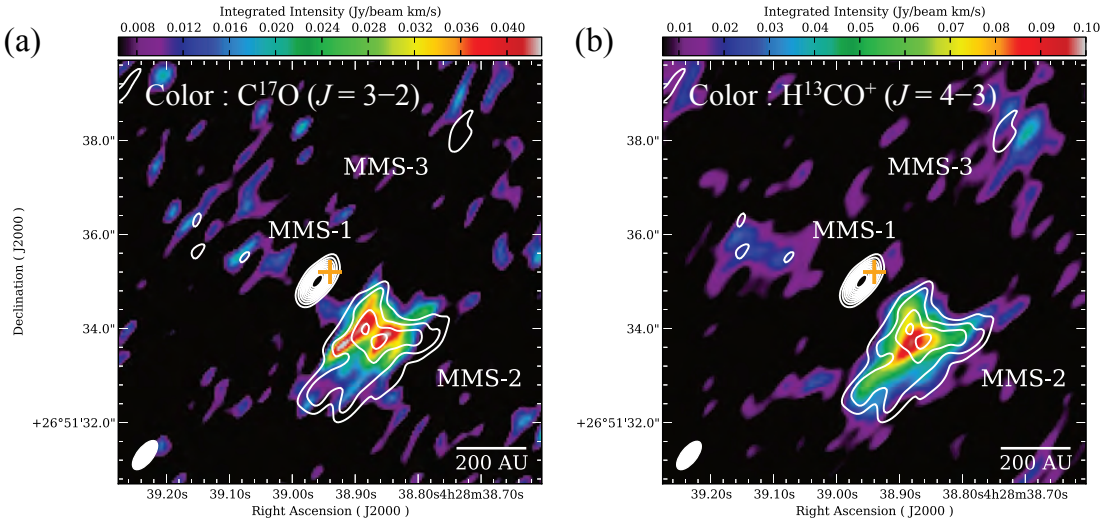

Fig. 1.— Gas/dust distributions of the high-density condensations of MC27/L1521F in Band 7 obtained by the 12-m array alone. (a) Total velocity-integrated intensities of $C^{17}O$ (J = 3–2) are shown in color scale. (b) Total velocity-integrated intensities of $H^{13}CO^+$ (J = 4–3) are shown in color scale. White contours represent the image of the 0.87 mm dust continuum emission in both (a) and (b). The lowest contour and subsequent contour step are 3σ and 2σ; 1σ ∼0.1 mJy beam^{-1}. The angular resolutions are given by the ellipses in the lower left corners in each panel, $0\farcs73 \times 0\farcs34$. Orange crosses in each panel represent the position of the *Spitzer* source.

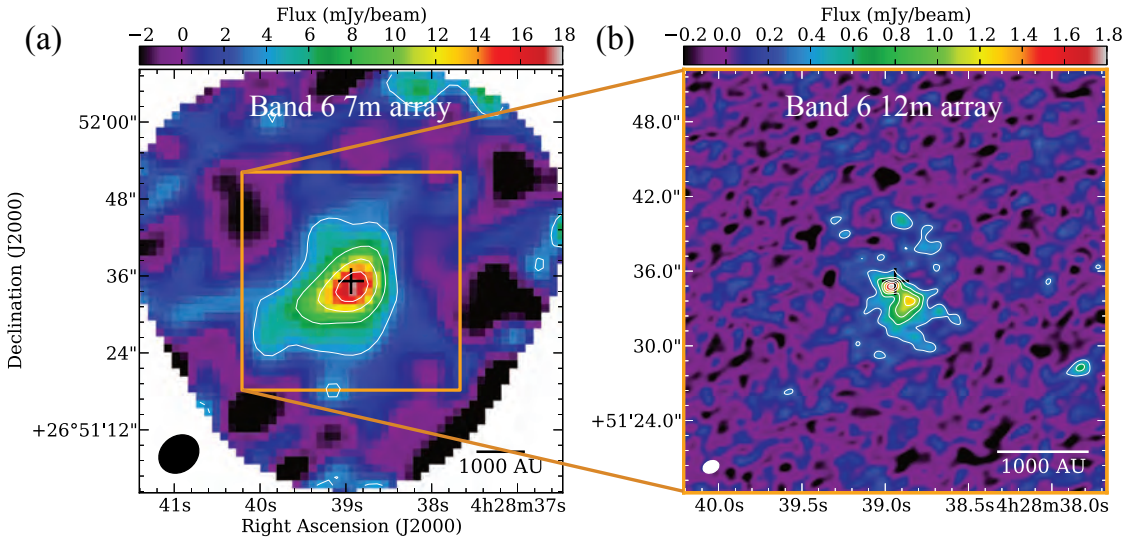

Fig. 2.— Distribution of 1.1 mm dust continuum emission toward MC27/L1521F. (a) Both color scale and contours show 1.1 mm dust continuum images obtained by the 7-m array. The lowest contour and subsequent contour step are 3.6 mJy beam^{-1}. (b) Both color scale and contours show 1.1 mm dust continuum images obtained by the 12-m array The lowest contour and subsequent contour step are 0.3 mJy beam^{-1}. The angular resolutions are given by ellipses in lower left corner of each panel. Black crosses in each panel represent the position of the *Spitzer* source.

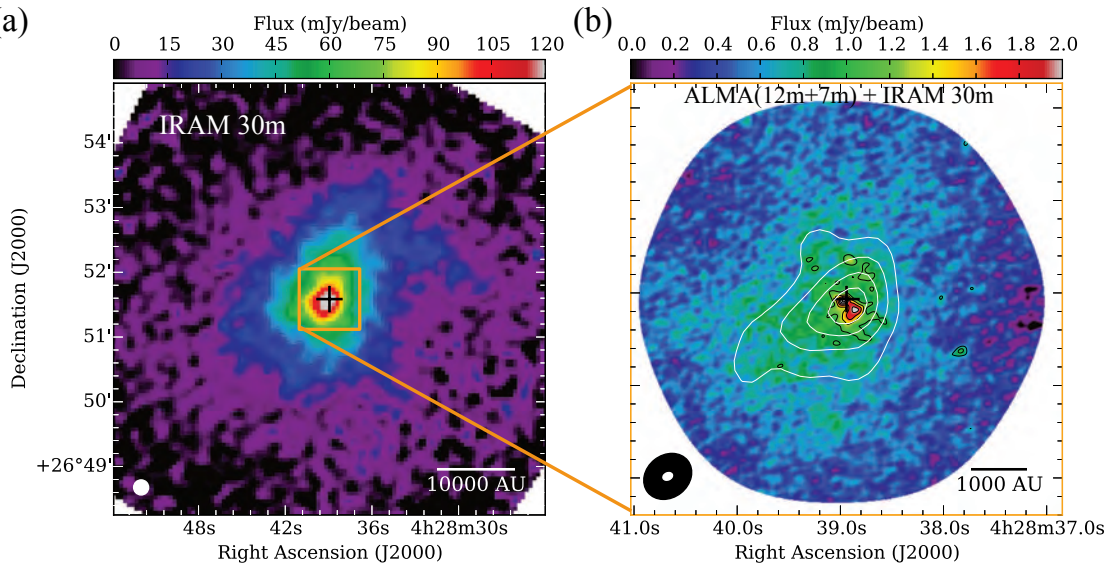

Fig. 3.— Distributions of dust continuum emission toward MC27/L1521F. (a) Color scale shows dust continuum image with the IRAM 30-m telescope using the MAMBO-2 bolometer at angular resolution of 14″. The angular resolution is given by the circle in the lower left corner. (b) Color scale image shows the dust continuum image combining the ALMA data (the 12-m array + the 7-m array) with IRAM 30-m data. Black and white contours illustrate 1.1 mm dust continuum emission taken by the 12-m array alone and the 7-m array alone, respectively. The contours start at three times the noise level and increase at this interval; the noise levels of the 12-m array data alone and 7-m array data alone are 0.10 mJy beam^{-1} and 1.2 mJy beam^{-1}, respectively. The black and white ellipses in lower left corner show the angular resolutions of the 7-m array data and the 12-m array data. Black crosses in each panel represent the position of the *Spitzer* source.

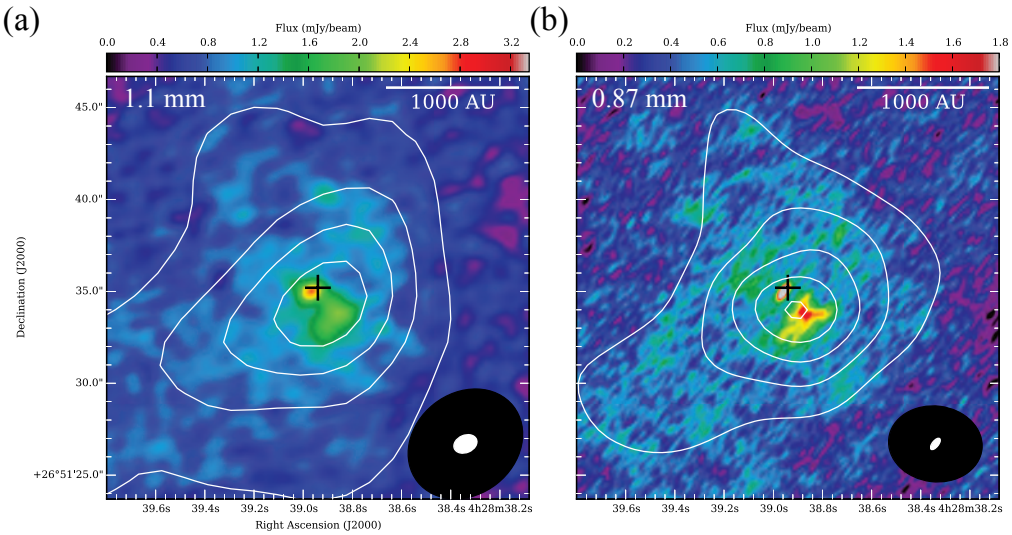

Fig. 4.— Distributions of dust continuum emission toward MC27/L1521F. (a) Color scale image shows 1.1 mm dust continuum image combining the ALMA data (the 12-m array + the 7-m array) with IRAM 30-m data same as Figure 3 (b). White contours illustrate 1.1 mm dust continuum emission taken by the 7-m array alone same as in Figure 2 (a). The angular resolutions of the combined image and the 7-m array alone are given by white and black ellipses, respectively, in the lower right corner. (b) Color scale image shows 0.87 mm dust continuum image combining the ALMA data (the 12-m array + the 7-m array) with JCMT/SCUBA data (Shinnaga et al. 2004; Kirk et al. 2005). White contours illustrate 0.87 mm dust continuum emission taken by the 7-m array alone. The contours start at three times the noise level and increase at this interval; the noise levels of the 7-m array data alone is 2.4 mJy beam^{-1}. The angular resolutions of the combined image and the 7-m array alone are given by white and black ellipses, respectively, in the lower right corner. Black crosses in each panel represent the position of the *Spitzer* source.

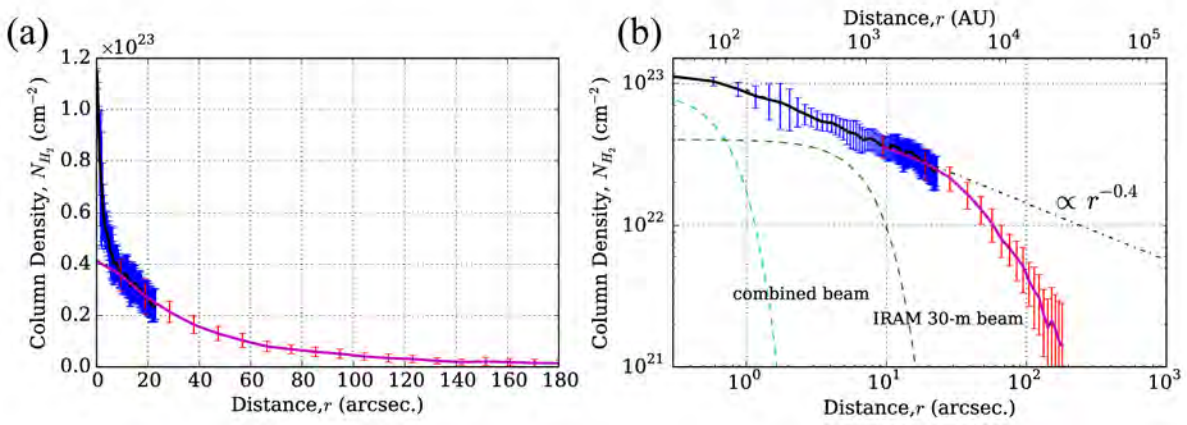

Fig. 5.— Mean radial profile of H_2 column density in MC27/L1521F made from dust continuum image obtained by the IRAM 30-m telescope alone and the combined ALMA data (the 12-m array + the 7-m array) with the IRAM 30-m data. Panel (a) and (b) show the linear-linear plot and the log-log plot of the profiles, respectively. The averaged profiles of the combined data and the IRAM data are shown by black and magenta solid lines, respectively. Blue and red bars show the ($\pm 1\sigma$) dispersion of the distribution of radial profiles in each data. The dash-dotted line in panel (b) denotes pure power-law distributions of $r^{-0.4}$. Dotted curves in green and cyan in panel (b) indicate beam shape of IRAM 30-m telescope image and the combined image, Gaussian function with FWHM of $14''$and $1''.1$, respectively.

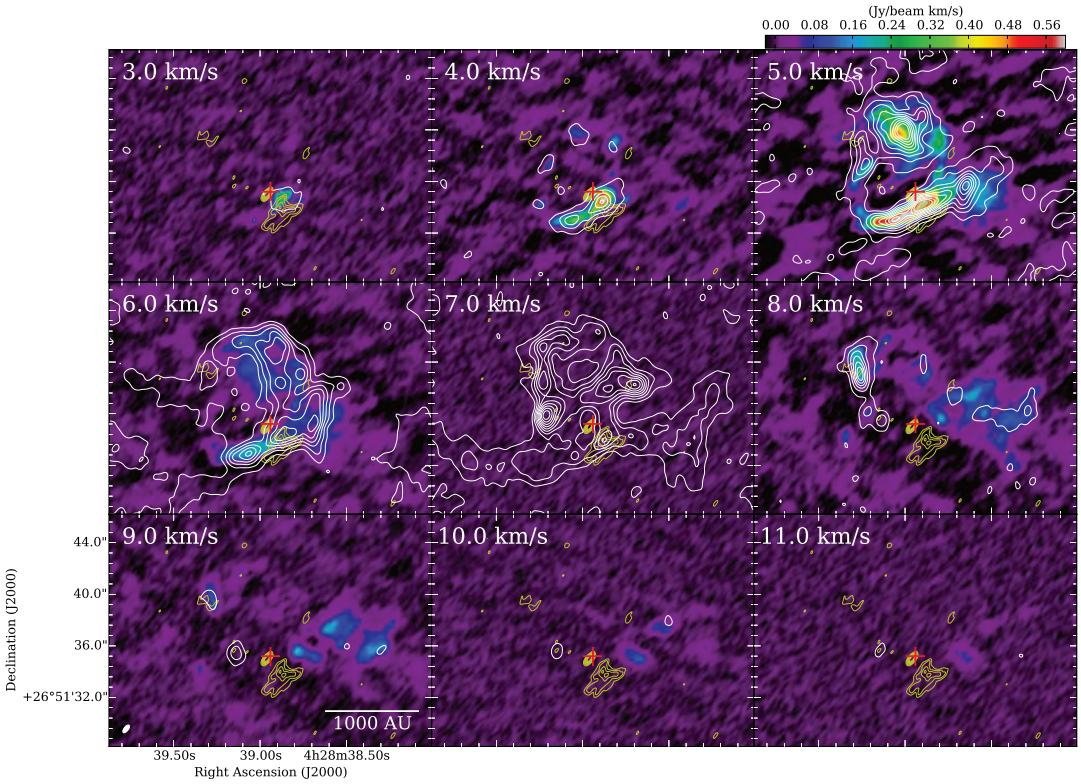

Fig. 6.— Velocity-channel maps of the ^{12}CO ($J = 3$–2) and HCO$^+$ ($J = 3$–2) emission toward MC27/L1521F. Color scale and white contours show velocity-range-integrated intensity maps of ^{12}CO ($J = 3$–2) data and HCO$^+$ ($J = 3$–2) data (Tokuda et al. 2014), respectively. The lowest contour and subsequent contour step are 0.02 Jy beam^{-1} km s^{-1} and 0.04 Jy beam^{-1} km s^{-1}, respectively. The velocity span for each map is 1.0 km s^{-1}. The lowest velocities are given in upper left corner of each panel. Yellow contours show the image of 0.87 mm dust continuum emission same as Figure 1. The angular resolution of the ^{12}CO ($J = 3$–2) is given by the white ellipse in the lower left corner of the bottom left panel, $0\farcs73 \times 0\farcs33$. Red crosses of each panel represent the position of the *Spitzer* source.

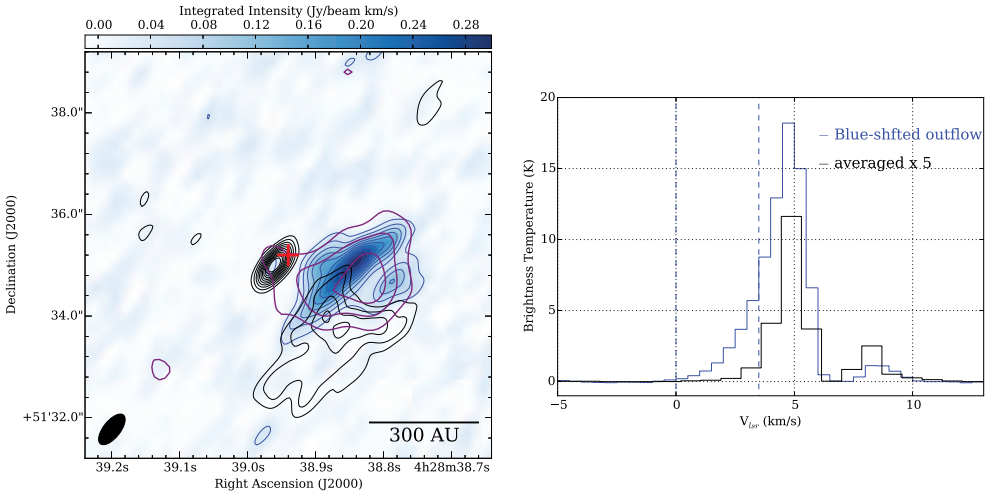

Fig. 7.— Distribution of blueshifted outflow from the *Spitzer* source. (a)The blue-color scale image and blue contours show images of velocity-integrated intensity of ^{12}CO (J = 3–2) with a velocity range of 0.0–4.0 km^{-1}. The lowest contour and subsequent contour step are 0.03 Jy beam^{-1} km s^{-1}. Black contours show the image of 0.87 mm dust continuum emission same as in Figure 1. The angular resolution of the ^{12}CO (J = 3–2) is given by the black ellipse in the lower left corner of the bottom left panel, 0.″73 x 0.″33. Red cross represents the position of the *Spitzer* source. Purple contours show images of velocity-integrated intensity of HCO$^+$ (J = 3–2) with a range of 0.0–4.0 km^{-1}. (b) Blue and black profile show averaged spectra over the regions inside the blue lowest contour and a circle of with a radius of 9.″0 at the center position of ($\alpha_{J2000.0}$, $\delta_{J2000.0}$) = ($4^{\rm h}28^{\rm m}38\overset{\rm s}{.}80$, +26°51′38.″3), respectively. Blue dashed line shows the velocity range for blue contours in panel (a).

Table 1. Beam sizes and sensitivities

	Band 6		Band 7	
Parameters	12-m array	7-m array	12-m array	7-m array
Synthesized beam size	$\sim 1\farcs3 \times 0\farcs8$	$\sim 6\farcs6 \times 5\farcs5$	$\sim 0\farcs32 \times 0\farcs74$	$\sim 5\farcs1 \times 4\farcs2$
Sensitivity of continuum observation (r.m.s.)	$\sim$0.1 mJy beam^{-1}	$\sim$1.2 mJy beam^{-1}	$\sim$0.1 mJy beam^{-1}	$\sim$2.4 mJy beam^{-1}
Sensitivity of line observation (r.m.s.)[a]	$\sim$7 mJy beam^{-1}	$\sim$50 mJy beam^{-1}	$\sim$5 mJy beam^{-1}	$\sim$30 mJy beam^{-1}

[a]The velocity resolutions of the Band 6 and the Band 7 are $\sim$1.0 km s^{-1} and $\sim$0.85 km s^{-1}, respectively.

Table 2. Derived parameters of 0.87 mm dust sources

Source	α (J2000)	δ (J2000)	F_ν (mJy)[a]	Size (AU)[b]	$F_{\rm max}$ (mJy beam^{-1})	$N_{\rm max}$ (cm^{-2})	$M_{\rm total}$ ($M_\odot$)
MMS-1	$4^{\rm h}28^{\rm m}38\fs96$	$+26^\circ51'35\farcs0$	2.6	—	2.7	—	—
MMS-2	$4^{\rm h}28^{\rm m}38\fs89$	$+26^\circ51'33\farcs9$	11.8	360	1.1	1.3×10^{23}	3.9×10^{-3}
MMS-3	$4^{\rm h}28^{\rm m}38\fs72$	$+26^\circ51'38\farcs0$	0.3	35	0.4	5.1×10^{22}	1.8×10^{-4}

[a]Flux of the dust emission integrated above the 3level (1σ rms $\sim$0.1 mJy beam^{-1})

[b]Diameter of a circle having the same area above 3level after deconvovled with the synthesized beam.